JOURNAL OF GUIDANCE, CONTROL, AND DYNAMICS
Vol. 25, No. 4, July–August 2002

Experimental Modal Analysis and Damping Estimation for an Inflated Thin-Film Torus

D. Todd Griffith and John A. Main
University of Kentucky, Lexington, Kentucky 40506

Experimental modal testing of an inflated torus is examined. The principal focus of this investigation is an evaluation of the use of conventional dynamic testing tools in modal testing of a thin-film inflated structure. Because thin-film structures are inherently flexible and lightweight, precautions must be taken in the test procedure. Challenges in testing and identifying natural frequencies and modal damping are detailed. The experimental study shows that whereas localized flexible body dynamics is predominant at higher frequency, the structure behaves in a fashion similar to that of a solid elastic structure for the low-order modes. In addition, natural frequencies and modal damping are shown to be dependent on the level of internal pressurization. Furthermore, viscous (air) damping and structural (strain-rate) damping coefficients are estimated from the experimentally measured modal parameters to provide a more complete assessment of the damping behavior of this structure.

Introduction

INFLATED structures are receiving a great deal of attention due to the need for low-cost space missions and the potential to improve greatly capabilities in a variety of applications. Inflated structures are a practical choice for deployment of very large aerospace structures. A large inflated structure can be stowed in a compact configuration and deployed on a single launch. The result is reduction in stowage space and launch cost and an orbital structure with unique capabilities.

One downfall of inflated structures is the loss of structural integrity that can result when the structure is pierced by an impact with high-velocity micrometeorites and space debris on orbit. To improve the survivability of inflated structures, various methods have been attempted to stiffen the structure through rigidization. The concept of rigidization can be approached in two primary ways: 1) the shell of the structure can be stiffened or 2) the enclosed gas can be replaced by a more rigid compression element. The stiffening of shell material can be accomplished by constructing the shell of the structure with a fabric/resin system.[1,2] With the fabric/resin approach, the key point in the design is the selection of a resin material that remains wet until deployed on orbit. Once in orbit, the structure is deployed, and the resin material can be cured by, for example, solar heating or humidification. Replacing the enclosed gas with a rigid foam has also been explored.[3,4] With this approach, thin-film inflatables can be stiffened by the injection of a liqueous foam into the structure once deployed. The liqueous foam expands to fill the structure and then hardens to form a rigid composite.

Typical inflated structure designs incorporate two structural support components, a circular or elliptical torus and a set of support struts that extend from the instrumentation housing of the spacecraft to the torus. Figure 1 shows a photograph of a prototype solar concentrator with the torus/lens and support strut configuration. The dynamic behavior of the inflated torus is of practical interest to spacecraft systems and structural design because the torus element is a key component of many inflated structure designs.[5–11] Inasmuch as it serves as structural support for an optical system such as a thin-membrane reflector or Fresnel lens, the inflated torus substructure is important to emerging space technologies that require solar energy acquisition for solar thermal propulsion and electrical power generation in orbital vehicles and solar sails. A visualization of a

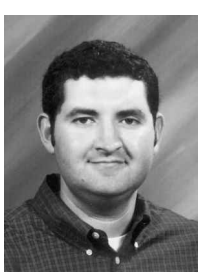

Todd Griffith received a B.S. in physics from Morehead State University and in mechanical engineering from the University of Kentucky in 1998. He received a M.S. in mechanical engineering from the University of Kentucky in 2000. His technical interests are in the general areas of dynamics and control of flexible structures and system identification. He is currently a Graduate Research Assistant at Texas A&M University. He is a Student Member of AIAA.

John Main received a B.S. in physics and mathematics from Western Kentucky University in 1984 and M.S. and Ph.D. degrees in mechanical engineering from Vanderbilt University in 1987 and 1993. He held a postdoctoral research position at Vanderbilt University from 1993 to 1995 and was a faculty member at the University of Maine from 1995 to 1997. In 1997 he joined the Department of Mechanical Engineering at the University of Kentucky. His technical interests are in the general areas of smart structural design and control, design of extremely large space telescope primary mirrors, shape control of thin-film mirrors, and inflated aerospace structures. He is a Member of AIAA.

Received 17 July 2001; revision received 30 September 2001; accepted for publication 21 November 2001.

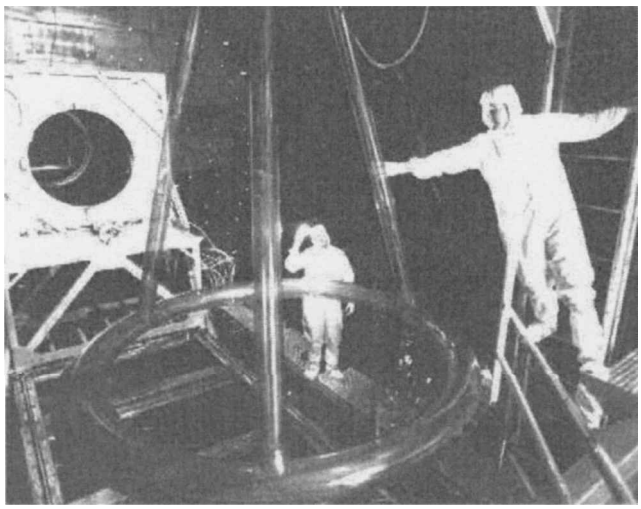

Fig. 1 Prototype solar concentrator in test facility (courtesy NASA Marshall Space Flight Center).

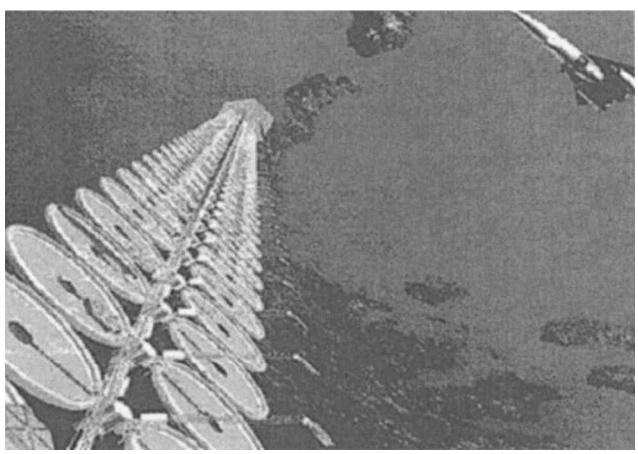

Fig. 2 Potential solar power application (courtesy NASA Marshall Space Flight Center).

potential application in solar power generation is shown in Fig. 2. Figure 2 shows a series of inflated ring-type structures on the arm of a large orbiting spacecraft.

A considerable amount of work has been done in the area of structural design of inflated structures; however, the work performed in the area of structural analysis is limited. Experimental investigations of the structural dynamics of inflated structures have been performed in both ambient and vacuum conditions,[12–15] as well as in zero-gravity conditions.[12] These reports detail the challenges experienced in testing thin-film inflated structures. In addition, some work in analytical modeling of the natural frequencies[12,14] and damping behavior[12] of inflated beams has been performed. Experimental investigations have also been performed on solid steel toroids[16] and thin-walled aluminum toroidal shells.[17] These reports are instructive in that they describe some of the important dynamic characteristics of the torus; however, the analysis was performed on stiffer, more conventional structures than that studied in this work. The use of noncontacting methods for measuring structural response has been studied.[13] Noncontacting methods are advantageous for highly flexible, ultralightweight structures in that accelerometer mass loading effects and stiffness of instrumentation wiring can be avoided. However, in this paper we evaluate modal testing of inflated structures using conventional contacting measurement and excitation techniques.

Accurate knowledge of structural dynamics is very important to structural design and structural control of any spacecraft structure. Further refinements in inflated structure design require assessment of inflated structure dynamics. This includes refining testing methodologies and modeling approaches so that the dynamics of spacecraft that incorporate inflated structure concepts can be better assessed. The objective of this paper is to present results from an experimental investigation that provides 1) a modal test approach using conventional modal testing tools and 2) a database for a structural modeling effort, as well as a description of the structural characteristics that should be included in a structural model.

Description of Test Article

The test article (fabricated by United Applied Technologies, Huntsville, Alabama) is a nonrigidized thin-film inflated torus with a 1.98-m ($2R = 6.5$ ft) major diameter and a 15-cm ($2r = 5.87$ in.) minor diameter (Fig. 3). The torus panels were thermally formed from flat sheets of the polyimide film Kapton HN®. Six thermally formed panels like the one in Fig. 4 make up the torus. Each thermally formed panel accounts for one-half of the structure's cross section and 120 angular degrees. Three thermally formed panels are joined end to end with epoxy to complete one-half of the structure. Two three-panel halves are joined to complete the torus. The method of fabrication results in variations in the thickness in the joining regions. A list of the structure's physical properties is given in Table 1.

Table 1 Physical parameters of test article

Property	Value
Modulus of elasticity	2.5 GPa (370,000 psi)
Density	1.42 g/cm^3 (0.051 lb/in.^{3})
Shell thickness	46 μm (1.8 mil)
Joining region width	5.1 cm (2 in.)
Joining region thickness (inner/outer)	360/150 μm (14/6 mil)

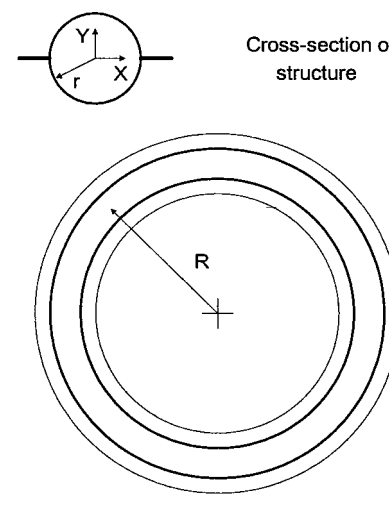

Fig. 3 Test article and cross section.

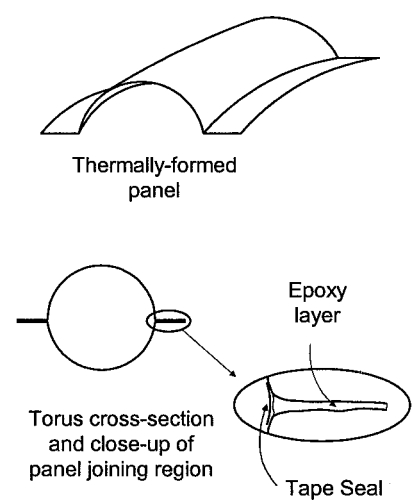

Fig. 4 Thermally formed panels used in torus construction and closeup of joining region.

Epoxy adds mass and stiffness to the structure in the bonded joints. Figure 4 includes a closeup of the joining region, which describes the variations in thickness in the bonded joints.

Modal Test Description

The objective of the experimental investigation was to evaluate modal test procedures for lightweight inflated structures. The goal was successful identification of the natural frequencies and damping of the first three in-plane and out-of-plane bending modes.

A number of issues related to the extreme flexibility and ultralightweight nature of inflated structures create challenges in performing modal tests. The key issues that must be addressed in the test procedure are listed as follows: 1) Reduce the mass loading effect of accelerometers by measuring frequency response functions (FRFs) with low-mass accelerometers. 2) Reduce the gravity effect by orienting accelerometers perpendicular to the gravity field. 3) Provide global excitation to structure using a modified impact hammer tip. In addition, internal pressurization should be varied to determine the effect of the shell prestress on natural frequency and damping. Each of these issues is addressed in more detail in the following sections.

FRF Measurement

The structure was tested in ambient laboratory conditions in two test configurations to determine the modal parameters for the in-plane and out-of-plane bending modes. In-plane testing was performed with the test article freely suspended parallel to the floor, whereas out-of-plane testing was performed with the test article freely suspended in a vertical position (Fig. 5). Monofilament line was used to hang the test article. Three monofilament strands were used for in-plane testing, whereas a single strand was utilized for out-of-plane testing. The strands were kept as long as possible (~2 m for the in-plane configuration) to minimize the frequency of the pendulum rigid-body mode (~0.3 Hz). For the out-of-plane test configuration, the strands used to hang the structure could not be greatly lengthened considering the space available; however, the pendulum mode for this configuration was below 1 Hz.

For in-plane testing, the inflated torus was excited with an impact hammer at a location on the outer surface of the structure near the joining region. The impact was directed in the plane of the structure in the radial direction. Acceleration was measured by roving an accelerometer, taking measurements at 16 evenly spaced points along the inner surface of the structure in the radial direction. For out-of-plane testing, the inflated torus was impacted in a direction perpendicular to its plane with 16 evenly spaced roving acceleration measurements taken in the same direction. Figure 6 shows details of the input and output measurement locations and directions. Two or three measurement locations would have been sufficient to characterize frequency and damping; however, 16 measurements results in adequate description of the mode shapes for the first three bending modes in both configurations, in plane and out of plane. Measurements were taken with low-mass (1.1-g) accelerometers with excitation repeated at a single point. Mounting coins (~1.5 g) were used to orient the accelerometers on the curved surface of the torus. FRFs were recorded with a laptop computer and a Zonic Medallion Mobile Fast Fourier Transform Analyzer (Model 2300) eight channel data acquisition system.

The mass of an accelerometer is a concern because the structure is extremely flexible. However, using low-mass accelerometers and the taking measurements in a direction perpendicular to the gravity field minimizes any mass loading effects. Also, the stiffness of the accelerometer lead was a concern because the structure was freely suspended. Therefore, the leads were also suspended with monofilament to minimize their effect on the measurements.

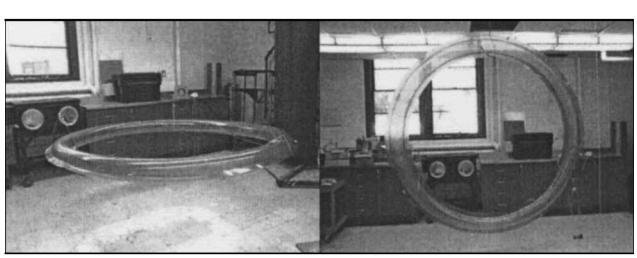

Fig. 5 Photographs of test orientations: a) in plane and b) out of plane.

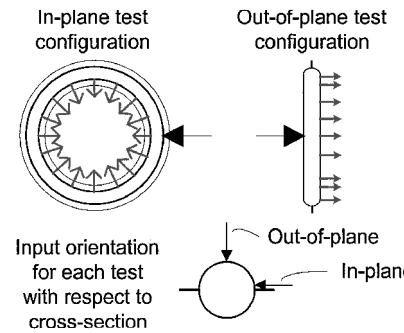

Fig. 6 Measurement locations and directions.

The structure was tested at two inflation pressures, 5.52 kPa (0.8 psig) and 6.89 kPa (1.0 psig), to examine the influence of shell prestress on the modal parameters. Air was supplied to the structure using a small aquarium pump, and pressure was maintained with the use of a controller capable of maintaining the pressure to within 0.34 kPa (0.05 psi) of the desired value. The gas supply system remained on during testing to compensate for leaks and maintain the desired constant pressure. Any effect of the pump on measured FRFs was expected to show up at 60 Hz (the pump diaphragm frequency). No such result was found.

In addition to pump noise, the flow of air into the structure could be considered an additional, nonquantified input. Leak rates were small enough that resupply was only needed every 30 s to maintain the desired pressure. Because the time period of one measurement was only 0.5 s, it was possible to take measurements when the pump was not in operation. Replacement airflow into the structure and leakage from the structure did not noticeably effect the measurement of FRFs in these tests.

Excitation Method

Because impact hammer testing is a common form of excitation in modal testing, it was decided to evaluate its utility in excitation of inflated structures. Attempts were made initially to excite the structure with common impact hammer tips such as small aluminum and rubber tips. It was found that these tips were too stiff and did not provide sufficient global excitation to the structure. The small hammer tips resulted in local deformation, which only excited local shell modes of the thin-film structure.

Further attempts were made with a hammer configuration incorporating a rectangular piece of aluminum measuring 3.81 cm (1.5 in.) in width and 10.2 cm (4 in.) in length. This modification was made to distribute the impact energy to a larger area of the structure's surface. Figure 7 shows the modified hammer tip used in the inflated structure tests. This hammer configuration provided sufficient energy distribution and minimized any type of local excitation, while exciting the global bending modes of the structure. Improvement in excitation with the modified hammer configuration was more profound in the case of out-of-plane testing. Here, the excitation is applied to the most flexible portion of the structure, the outer curved surface. For in-plane testing the impact is near the joining region, where the structure is stiffer; however, distributing the impact energy in this fashion also improved the measurement for the in-plane tests.

For any modal test, it is highly desirable that there be a strong correlation between the quantified input and the measured output. The coherence function, or simply coherence, gives a measure of the input–output relationship and can be simply defined as the square of the correlation coefficient between the input and output signals as a function of frequency.[18] Coherence was used primarily to determine the effectiveness of each impact excitation in these tests. The coherence was viewed after each successive impact. Any sharp decrease in coherence broadband indicated poor excitation, and so the measurement was removed and repeated.

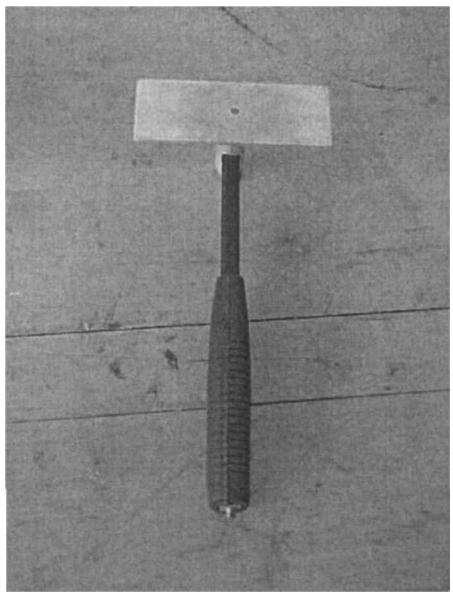

Fig. 7 Modified impact hammer configuration.

In addition, coherence was noted to be sensitive to input force level. The measured coherence was improved for lower force levels. In these tests, the acceptable input force level range was determined by softening the impact until the measured coherence was optimized. The requirement for a suitable impact was a force input range of 2–5 N (0.45–1.12 lbf) for the out-of-plane excitation and 3–12 N (0.67–2.69 lbf) for the in-plane excitations. Higher force levels for the in-plane excitation are acceptable because the structure was impacted near the seam, a stiffer portion of the structure. Additional information on coherence measurement for these tests is detailed later in this report.

Discussion of Modal Test Results

X-Modal (version 2, developed by the Structural Dynamics Research Laboratory, University of Cincinnati) was used to perform the system identification. Essentially, X-Modal builds a linear system model of the structural dynamics. The software was used to determine a consistency diagram from the FRF data, which were used to identify the natural frequencies and damping values and to assess the variation of the modal parameters with system model order. The polyreference time domain algorithm was chosen to perform the system identification. In this approach, the desired model orders for the system identification are user specified. In addition, the highest model order chosen should be sufficient to capture the order of the system. In addition, frequency and damping estimates were obtained using both H_1 and H_2 FRFs to obtain a better estimate of the modal parameters.

Identification of Natural Frequencies

Natural frequencies were identified using the consistency diagrams, FRFs, and mode shape plots. Certainly, this is a common and elementary procedure for determining frequency and damping information; however, for a thin-film inflated structure, it is necessary to consider all available information in the identification process. Therefore, we go into greater detail than is usually warranted for this type of analysis to present more completely the dynamics of this nontraditional structure.

A stable column of poles on the consistency diagram indicates that there is a high-energy mode at that particular frequency. The plots in Figs. 8 and 9 are consistency diagrams for the in-plane test at a pressurization of 5.52 kPa (0.8 psig) for H_1 and H_2 estimates, respectively. These diagrams show three strong peaks near 15, 40, and 60 Hz with corresponding columns of complex poles (denoted by an inverted triangle on the consistency diagram) at a near-constant frequency for increasing system model order.

The use of FRFs to identify natural frequencies is inadequate due to noisy measurements that result from localized shell mode

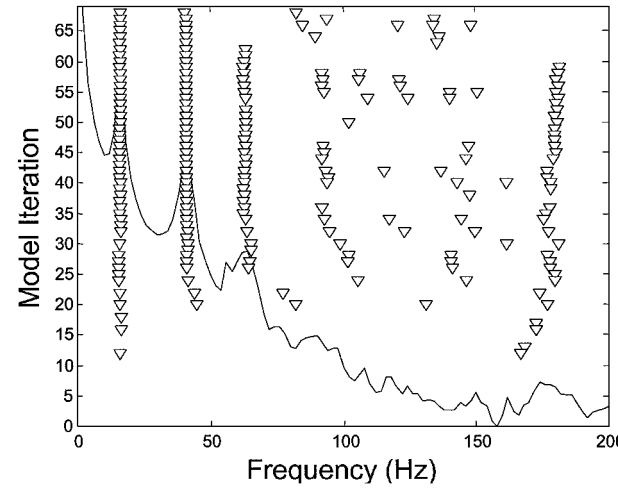

Fig. 8 Consistency diagram for in-plane configuration at 5.52 kPa using H_1 estimate.

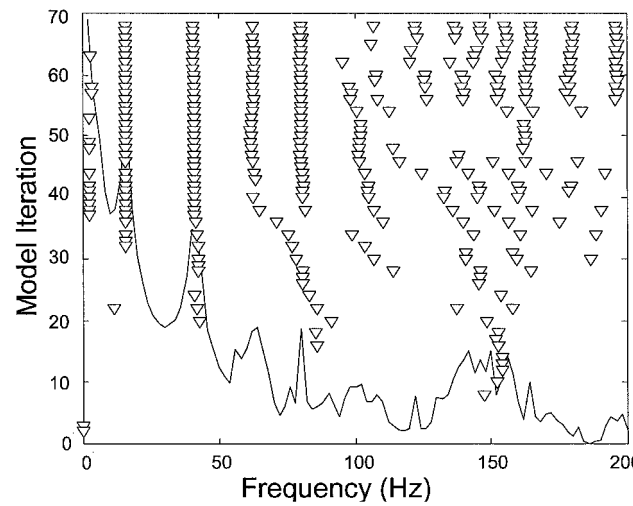

Fig. 9 Consistency diagram for in-plane configuration at 5.52 kPa using H_2 estimate.

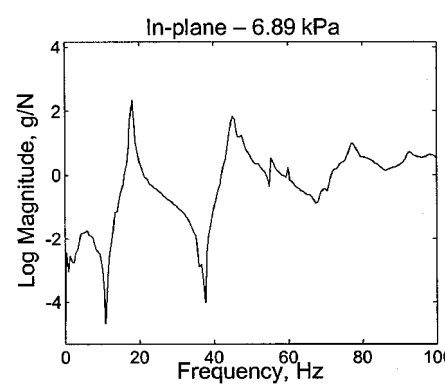

Fig. 10 Drive point FRF for in-plane configuration.

activity. Figures 10 and 11 show typical drive point FRFs for the in-plane and out-of-plane configurations, respectively. In a strict sense, these are not true drive point measurements because the acceleration measurements were taken at points 180 deg about the cross-section from the input location, therefore, some degree of flexibility exists between the input and output. Figure 10 is a drive point FRF for the in-plane configuration at 6.89 kPa (1.0 psig). Figure 10 shows distinct resonance peaks for the first two natural frequencies (near

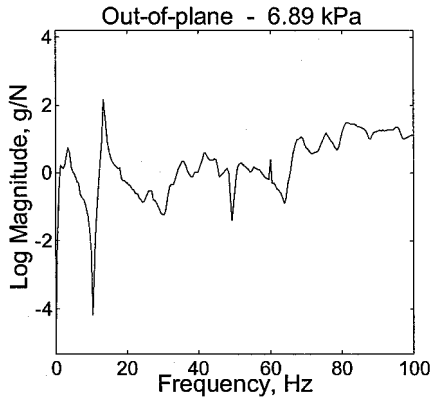

Fig. 11 Drive point FRF for out-of-plane configuration.

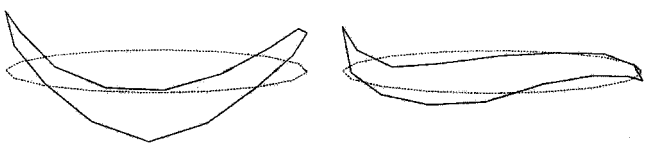

First **Second**

Fig. 12 Experimental mode shapes for out-of plane bending modes.

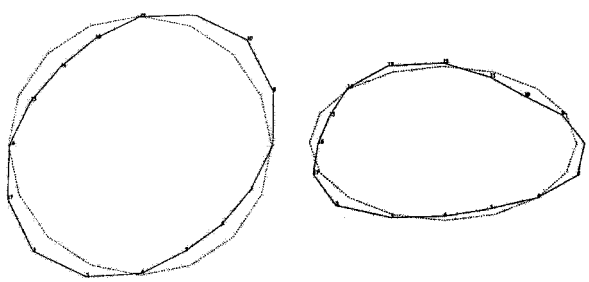

a) First **b) Second**

Fig. 13 Experimental mode shape plots for in-plane bending modes.

18 and 45 Hz). The resonance peak near 80 Hz is the third in-plane bending mode, which is less easily identified because there is a large amount of shell mode activity at this frequency.

Figure 11 is a drive point FRF for the out-of-plane configuration at 6.89 kPa (1.0 psig). Figure 11 only shows one distinct peak at the first bending mode near 13 Hz and shows that higher-order bending modes are not easily discernible when a large amount of shell mode activity is present at a higher frequency. As expected, the abundance of shell mode activity is larger for the out-of-plane test because the acceleration measurements were taken on the most flexible outer curved surface of the structure. A comparison of Figs. 10 and 11 shows that FRFs are generally more easily discernible when exciting and recording measurements at a more stiff location on the structure. With a large amount of localized shell mode activity, it is difficult to determine higher-order bending modes from FRFs alone. For this reason, the use of mode shapes is of great importance to the identification of global bending modes. The FRFs indicate the frequency at which shell modes begin to become important. For these tests, shell modes dominate the structural dynamics above 50 Hz for the in-plane test and above 30 Hz for the out-of-plane test.

Shell mode activity in the frequency band of global bending modes tends to obscure the identification of natural frequencies. Therefore, mode shape plots are a key piece of information in identifying the bending modes. Analytical circular ring models[19] offer a good approximation of the mode shapes for the inflated torus for the purpose of comparison with experimental mode shapes. The first two experimental mode shapes for each configuration are given in Figs. 12 and 13. Figure 12 shows the first two out-of-plane bending modes, and Figure 13 shows the first two in-plane bending modes. (Note that in Fig. 13b that the mode shape plot for the second bending mode is shown in an isometric view.) The mode shapes for a circular ring model given in Ref. 19 show good agreement with those in Figs. 12 and 13; therefore, we can confirm that these modes correspond to the desired bending modes.

In addition to structural response, the pneumatic response of the enclosed gas should also be considered.[17] Pneumatic resonance can be predicted using the famous relation for speed of sound, frequency, and wavelength (speed of sound is equal to frequency times wavelength). The speed of sound in air at atmospheric pressure (101.3 kPa) and 21°C (70°F) is 344 m/s. The wavelength associated with the fundamental harmonic pneumatic resonance is the mean circumference of the inflated torus (6.2 m). With these values for speed of sound and wavelength, the fundamental harmonic pneumatic resonance frequency is estimated to be 55.3 Hz. An inspection of the consistency diagrams of Figs. 8 and 9 shows that there is a small peak near this frequency to the left of the third dominant column of poles in each figure. We cannot say with certainty that this is a pneumatic response of the enclosed gas. However, note that the fundamental pneumatic response and higher-order harmonics are likely to be found in the frequency band of interest. The precise frequency at which pneumatic resonance will occur will depend on, as shown here, the speed of sound and the wavelength of the mode of interest. A test to identify pneumatic resonance could include using different inflation gases with distinctly different speeds of sound, or, if possible, testing structures with different length/diameter. In this report, we made no attempt to identify pneumatic resonance.

Several modal tests were performed in each configuration at two different pressures. The natural frequencies (bending modes) and damping identified from modal parameter estimation for each of these tests are listed in Tables 2 and 3. A description of how the modal damping values in Tables 2 and 3 were determined is given in the next section. At higher pressurization, the increase in stiffness is larger than the increase in mass associated with the higher internal pressurization; therefore, the natural frequencies increased with increasing pressure. This result is found for both the in-plane and out-of-plane bending modes. For a 25% increase in pressure (from 5.52 to 6.89 kPa), the out-of-plane natural frequencies increased by 1.7, 9.1, and 2.3%, whereas the in-plane natural frequencies increased by 12.9, 13.3, and 27.6%, respectively, for the first three bending modes in each configuration based on the H_1 estimation. Furthermore, the in-plane bending frequencies are higher than the out-of-plane bending frequencies. This effect is due to the additional in-plane stiffness due to the joining regions. In addition, it is shown that modal damping follows the opposite trend with lower modal damping ratios for a higher pressurization level with the exception of the second out-of-plane mode at 6.89 kPa (1.0 psig). The departure of the modal damping of this mode from the general trend was evident in a subsequent modal test, and, as well, the latter value was consistent with the reported value. This indicates that either the damping for this mode is simply unusually high, or that possibly some other mechanism, that is, excitation of other modes such as in-plane bending by out-of-plane impact, contributes to the response of the second out-of-plane mode at 6.89 kPa. There is no evidence that the in-plane and out-of-plane modes were coupled in these tests; therefore, it is most likely that the damping for this mode simply deviates from the trend.

Damping Estimation

Identifying the natural frequencies of the first three bending modes is a straightforward task; however, determination of the damping values for each mode requires more attention. For each configuration and pressurization level, the modal analysis was performed using two FRF estimation approaches, the H_1 and H_2 estimates.[18] H_1 tends minimize the error of the output and results in underestimation of the amplitude at resonance and overestimates the damping values, whereas H_2 tends to minimize the error of the input and results in overestimation of the amplitude at resonance and underestimates the damping values.[20] Therefore, it should be expected that a damping range can be determined using both FRF estimates. Because the damping values vary significantly with system model order, a range of model orders in which the damping values became most consistent was chosen to estimate the percent damping. For each mode, the damping values, as well as the natural

Table 2 Natural frequencies and damping for in-plane bending

Mode	Model orders	H_1 estimate		H_2 estimate	
		Frequency, Hz	Damping, %	Frequency, Hz	Damping, %
		In plane: 5.52 kPa			
1	50–64				
	Average	16.00	1.50	15.92	1.55
	Standard deviation	0.02	0.50	0.02	0.76
	Range	——	0.94–2.12	——	0.47–2.68
Range for all model orders		——	0.23–2.54	——	0.38–10.14
2	50–64				
	Average	40.94	2.54	40.91	2.13
	Standard deviation	0.04	0.69	0.09	0.69
	Range	——	1.85–3.34	——	1.35–3.20
Range for all model orders		——	0.14–7.16	——	0.49–7.29
3	50–64				
	Average	63.20	4.79	62.54	2.96
	Standard deviation	0.32	4.06	0.45	1.96
	Range	——	1.79–15.28	——	0.35–5.26
Range for all model orders		——	1.46–15.28	——	0.35–5.91
		In plane: 6.89 kPa			
1	50–64				
	Average	18.07	1.11	18.05	1.13
	Standard deviation	0.02	0.18	0.01	0.22
	Range	——	0.94–1.37	——	0.90–1.55
Range for all model orders		——	0.38–3.36	——	0.57–2.83
2	50–64				
	Average	46.40	1.68	46.55	1.81
	Standard deviation	0.10	0.45	0.11	0.49
	Range	——	1.23–2.33	——	1.32–2.72
Range for all model orders		——	0.41–5.18	——	1.32–2.72
3	65–86				
	Average	80.65	2.13	80.73	2.60
	Standard deviation	1.33	2.72	0.84	2.72
	Range	——	0.10–8.71	——	0.08–7.39
Range for all model orders		——	0.10–8.71	——	0.08–7.39

Table 3 Natural frequencies and damping for out-of-plane bending

Mode	Model orders	H_1 estimate		H_2 estimate	
		Frequency, Hz	Damping, %	Frequency, Hz	Damping, %
		Out of plane: 5.52 kPa			
1	60–74				
	Average	13.30	3.39	13.31	4.38
	Standard deviation	0.04	0.66	0.05	0.97
	Range	——	2.66–4.15	——	3.37–5.43
Range for all model orders		——	1.32–8.32	——	0.16–12.09
2	80–94				
	Average	31.48	2.85	31.33	3.75
	Standard deviation	0.19	1.00	0.07	1.28
	Range	——	2.05–4.72	——	2.15–5.81
Range for all model orders		——	2.05–4.72	——	0.48–7.16
3	75–90				
	Average	64.71	4.05	64.78	3.94
	Standard deviation	0.21	0.86	0.24	0.65
	Range	——	3.18–5.39	——	3.22–4.92
Range for all model orders		——	1.84–5.97	——	1.10–6.44
		Out of plane: 6.89 kPa			
1	60–74				
	Average	13.53	1.39	13.71	0.84
	Standard deviation	0.01	0.25	0.01	0.14
	Range	——	1.07–1.76	——	0.65–1.02
Range for all model orders		——	0.31–9.68	——	0.31–7.60
2	80–94				
	Average	34.34	7.07	34.02	6.80
	Standard deviation	0.31	2.35	0.14	2.76
	Range	——	4.64–11.02	——	3.53–11.15
Range for all model orders		——	4.64–11.02	——	3.53–11.15
3	70–90				
	Average	66.21	3.55	64.57	3.67
	Standard deviation	0.47	2.63	0.34	2.63
	Range	——	0.54–6.43	——	0.22–6.81
Range for all model orders		——	0.54–6.43	——	0.22–8.19

frequencies, were averaged for a range of about 15 model orders. The same range of model orders was maintained for both the H_1 and H_2 estimates to draw a comparison between the two FRF estimation techniques. Again, the natural frequencies and damping values are listed in Tables 2 and 3 for each test configuration and pressurization level.

Given the high damping of this structure, a more conservative damping ratio estimate should be achieved using an H_2 estimate. However, an interesting result is found in this modal analysis in that the H_2 estimation technique does not always give a lower damping value estimate than the H_1 technique. An examination of the damping values shown in Tables 2 and 3 shows that the damping estimates for each technique are not significantly different in magnitude. In addition, the damping range for each technique is not significantly different statistically as shown by the standard deviation of the range of values.

Also of interest is estimation of the individual damping mechanisms that contribute to the experimentally determined modal damping. These damping mechanisms can include viscous (air) damping, structural (strain-rate) damping, spatial hysteresis, and time hysteresis.[21] However, we will only consider the time-independent viscous and structural damping. Estimation of viscous damping indicates something important regarding the influence of air damping for tests performed in the ambient environment. In addition, it provides another parameter to be included in a structural model. The ability to estimate the effect of structural damping would be very useful for an inflated aerospace structure because external viscous damping will not be present on-orbit. Cudney and Inman[22] have demonstrated that, for an Euler–Bernoulli beam, determining the individual effects of viscous and structural damping can be accomplished using the measured natural frequencies and modal damping. In essence, a linear least-squares solution is utilized to fit the measured modal parameters to an appropriate damping model based on the equation of motion for the structure.

In the interest of brevity, we will not present the full development, but only summarize the most important results. Assuming proportional damping, the following equation is found upon a modal expansion solution of the equation of motion. Equation (1) relates the experimentally determined modal parameters to the to-be-determined damping coefficients:

$$2\zeta_n\omega_n\mu = C + C_s I\beta_n^4 \tag{1}$$

Equation (1) is written here in general form and can be applied for both the in-plane and out-of-plane data sets. Here, ω_n and ζ_n are the experimentally determined natural frequency and damping ratio for the nth mode, μ is the mass per unit length about the torus circumference, I is the moment of inertia for the torus cross section, and β_n is the circular ring theoretical eigenvalue for the nth mode. C and C_s are the viscous and structural damping coefficients, respectively. Note that, due to the joining region, the moments of inertia for the in-plane and out-of-plane cases are different. Therefore, depending of whether the in-plane or out-of-plane modes are being studied, the value of I in Eq. (1) becomes either I_y (3.2×10^{-7} m^4) or I_x (4.9×10^{-8} m^4), respectively. The theoretical eigenvalues β_n are available from frequency expressions for a circular ring.[19]

Equation (1) is in x–y form with y represented by $2\zeta_n\omega_n\mu$ and x by $I\beta_n^4$. In this convenient form, the damping coefficients C and C_s are found from a least-squares fit of the set of experimentally determined natural frequencies, modal damping ratios, and theoretical eigenvalues. The regression yields the viscous damping coefficient C as the y intercept and the structural damping coefficient C_s as the slope of the regression.

The theoretical eigenvalues for in-plane and out-of-plane bending are given in Table 4. The fitting problem is approached using a weighted least-squares approach to account for measurement uncertainty.[23] Therefore, the weighting matrix W is chosen to have the form diag$(1/\sigma_n^2)$, where σ_n^2 is the variance of the nth modal damping ratio. In this way, the damping values that are known the best are given more importance in the regression. The problem is formulated as

$$\begin{bmatrix} C \\ C_s \end{bmatrix} = (B^T W B)^{-1} B^T W \begin{bmatrix} 2\zeta_1\omega_1\mu \\ 2\zeta_2\omega_2\mu \\ \cdot \\ \cdot \\ 2\zeta_n\omega_n\mu \end{bmatrix}, \quad \text{where} \quad B = \begin{bmatrix} 1 & I\beta_1^4 \\ 1 & I\beta_2^4 \\ \cdot & \cdot \\ \cdot & \cdot \\ 1 & I\beta_n^4 \end{bmatrix} \tag{2}$$

For the current problem, we only have three modes available for this regression. This is a limitation; however, the modal parameters fit well to this damping model with the exception of out-of-plane regression for a pressurization of 6.89 kPa (1.0 psig). The estimated viscous damping and structural damping coefficients are given in Table 5 along with the R^2 values for each fit. The regression plots are given in Figs. 14 and 15.

The modal damping for the second out-of-plane bending mode at 6.89 kPa (1.0 psig) was considerably higher than that of the first and third modes. This raises questions about the accuracy of the damping values for this data set; however, the uncertainty in this measurement was accounted for by using the weighted least-squares approach. This allows some general trends to be observed from the estimated damping coefficients in Table 5. Structural damping was generally higher for higher pressurization levels (higher film prestress). On the other hand, viscous damping follows the opposite trend with higher viscous damping at lower pressurization. In addition, modal damping for the out-of-plane bending modes (Table 3) was generally higher than those for the in-plane bending modes. This is not surprising because viscous damping is directly proportional to the amount of external fluid mass displaced. More fluid is

Table 4 Theoretical eigenvalues β_n for the in- and out-of-plane circular ring models

Mode	In plane	Out of plane
1	1.638	1.611
2	2.755	2.732
3	3.815	3.796

Table 5 Damping regression results

		H_1			H_2		
Configuration	Pressure, kPa	C, Ns/m^2	C_s, Ns/m^5	R^2	C, Ns/m^2	C_s, Ns/m^5	R^2
In plane	5.52	0.216	68,500	0.991	0.419	38,500	0.988
In plane	6.89	0.201	46,400	0.989	0.194	52,100	0.995
Out of plane	5.52	0.529	324,000	0.999	0.821	288,000	0.998
Out of plane	6.89	0.168	392,000	0.666	0.046	386,000	0.704

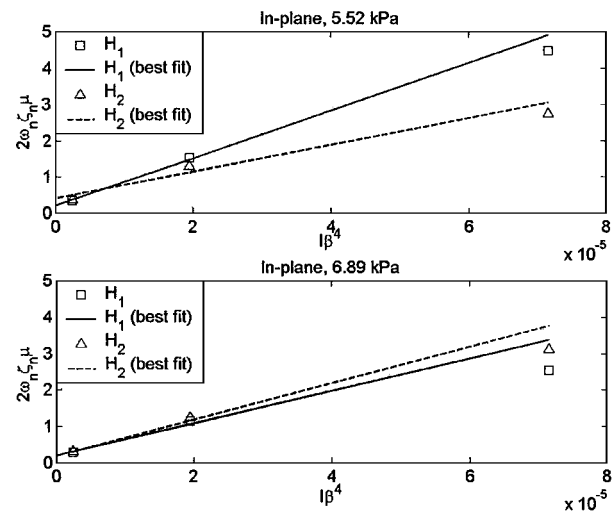

Fig. 14 Damping regressions in plane.

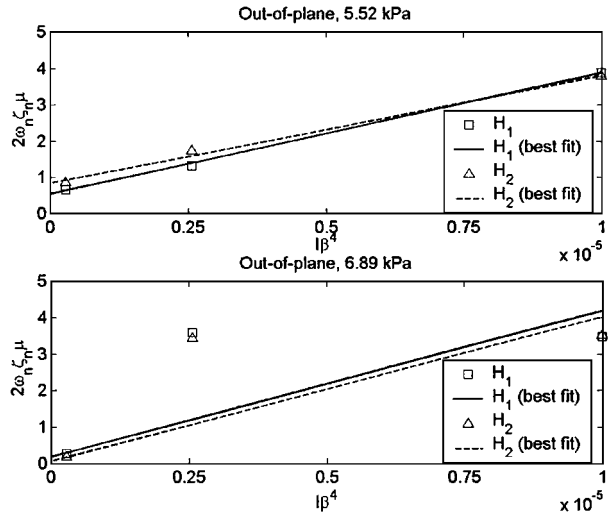

Fig. 15 Damping regressions out of plane.

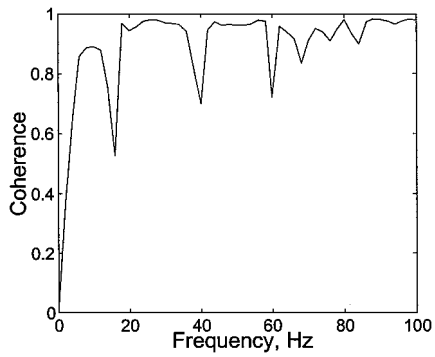

Fig. 16 Coherence at drive point for in-plane testing at 6.89 kPa.

displaced in out-of-plane bending because the joining regions will have a greater contribution to viscous damping than is the case for in-plane bending. Note that, if we had used a non-weighted least-squares approach to perform the damping estimation, we would find the estimated viscous damping coefficients to be higher, and in turn the structural damping coefficients would be lower than those reported in Table 5. This result was found for each configuration and pressurization level for both H_1 and H_2 estimates.

No attempt was made to determine the effect of temperature on the natural frequencies and damping in these tests with the temperature maintained at 21°C (70°F). However, in general, we can expect that temperature will have an effect on the properties of the shell material and the enclosed gas. For example, at lower temperature, we should expect the film material to stiffen, and the speed of sound of the enclosed gas will decrease. As a result, the natural frequencies should increase with higher structural damping and higher viscous damping, and the frequency of pneumatic resonance should decrease.

Coherence Measurement

Figure 16 is a drive point coherence plot for the test characterizing in-plane bending modes at a pressurization of 6.89 kPa (1.0 psig). The coherence is close to one broadband with the exception of the value at resonant frequencies. This could be the result of nonlinear behavior near resonance, but is more likely the result of a large output measurement corresponding to a small input. Because the input and output locations are not collocated, some flexibility exists between these points inasmuch as they are located at 180 deg about the structure's cross section. The large amplitude output measurement is likely due to the excitation of modes related to distortion of the cross section.

Figure 17 shows a similar plot of coherence at a lower pressurization level of 5.52 kPa (0.8 psig). At lower pressure, the structure

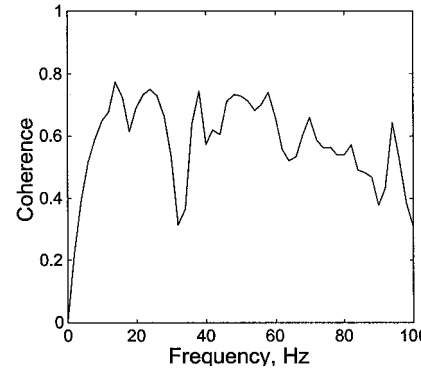

Fig. 17 Coherence at drive point for in-plane testing at 5.52 kPa.

is less stiff and more apt to wrinkle. The drop in coherence broadband indicates either that the structure behaves nonlinearly for the entire frequency range of interest or that in some way the suspension is providing input to the structure. Additional input from the suspension is not likely because a broadband drop in coherence was not found at the higher pressurization level. Therefore, the drop in coherence broadband at the lower pressurization level is most likely due to nonlinear behavior because more nonlinearity is expected at lower pressure levels, where the structure is more apt to wrinkle. These results indicate that the inflated torus begins to exhibit some nonlinearity below 6.89 kPa (1.0 psig). At higher pressure, the structure behaves more linearly, as indicated by Fig. 16.

Conclusions

Inflated structures have several interesting characteristics that contribute structural nonlinearities. A significant material nonlinearity is present because it has been observed in an experimental study that the dynamic modulus of prestressed films varies with frequency. Also, the method of gluing the panels that comprise the structure significantly impacts structural stiffness and structural damping. Another important structural characteristic of inflated structures is wrinkling, which is present in the loaded as well as unloaded state, due to imprecise joining of the thermally formed panels. At increasing pressurization, a considerable portion of the wrinkling is removed; however, when bending moments reach sufficient magnitude, the film will wrinkle.

This paper demonstrates that at least certain types of inflated aerospace structures can be successfully tested in ambient conditions. Conventional modal testing of inflated aerospace structures requires making efforts to reduce mass loading effects from the instrumentation, to reduce the gravity effect by orienting accelerometers perpendicular to the gravity field, and to avoid local excitation by distributing the impact over a larger contact area. The result of testing in ambient conditions is that air damping is present and will impact the structural dynamics. However, it has been demonstrated that even in the presence of air damping measured modal parameters can be used to estimate the individual viscous and structural damping effects. The ability to identify a larger number of modes would improve the accuracy of damping estimation. In addition, a study of time-dependent damping mechanisms may reveal some of the key structural dynamics of inflated aerospace structures. Estimation of these damping mechanisms is important with regard to the development of accurate structural models. In addition, an attempt was made to estimate modal parameters by H_1 and H_2 techniques. In theory, this approach would result in an upper and lower bound on the estimates for natural frequency and damping. However, for this study no such range could be established.

The full assessment of the effect of the enclosed gas on the structural dynamics of an inflated structure is still an open question. The results of this study have shown that natural frequencies and modal damping are dependent on the level of pressurization. For higher internal pressure, natural frequencies increase, whereas, in general, modal damping follows the opposite trend. In the orbital environment, external viscous damping will not be present. Therefore, an

important question that remains is what role does the enclosed gas play in the damping behavior of an inflated structure. The results of the present study for two pressurization levels indicate that structural damping is greater for higher internal pressurization. A more rigorous test protocol should be designed to ascertain the effects of pressurization level and internal and external viscous air damping. It is suggested that an inflated aerospace structure be tested at a minimum of three pressurization levels. In addition, testing a structure in both the ambient environment and in vacuum conditions would provide an important characterization of the damping behavior of these structures.

References

[1]Bernasconi, M., and Reibaldi, G., "Inflatable Space-Rigidizing Structures: Overview of Applications and Their Technology Impact," *Acta Astronautica*, Vol. 14, 1988, pp. 455–465.

[2]Bernasconi, M., "Inflatable Space-Rigidized Antenna Reflectors: Flight Experiment Definition," International Astronautical Federation, Paper IAF-88-049, 1988.

[3]Lester, D., and Cannon, D., "Foam Inflated Rigidized Truss Structure Developed for an SRF Technologies Solar Concentrator," Proceedings of the 1996 International Solar Energy Conf., American Society of Mechanical Engineers, March–April 1996.

[4]Griffith, D. T., and Main, J. A., "Structural Modeling of Inflated Foam-Rigidized Aerospace Structures," *Journal of Aerospace Engineering*, Vol. 13, No. 2, 2000, pp. 37–46.

[5]Dornheim, M. A., "Inflatable Structures Taking to Flight," *Aviation Week and Space Technology*, Jan. 1999, pp. 60–62.

[6]Freeland, R. E., "Significance of the Inflatable Antenna Experiment Technology," *Proceedings of the AIAA/ASME/AHS/ASC 39th Structures, Structural Dynamics, and Materials Conference and Exhibit and the AIAA/ASME/AHS Adaptive Structures Forum*, AIAA, Reston, VA, 1998, pp. 2789–2796.

[7]Covault, C., "USAF Shifts Technology For New Future in Space," *Aviation Week and Space Technology*, Aug. 1998, pp. 40–47.

[8]Tinker, M. L., "Passively Adaptive Inflatable Structure for the Shooting Star Experiment," AIAA Paper 98-1986, 1998.

[9]Ashley, S., "Rockets Powered by the Sun," *Mechanical Engineering*, Nov. 1997, p. 48.

[10]Chmielewski, A. B., "Overview of Gossamer Structures," *Gossamer Spacecraft: Membrane and Inflatable Structures Technology for Space Applications*, edited by Christopher H. M. Jenkins, Progress in Aeronautics and Astronautics, AIAA, Reston, VA, 2001, pp. 1–33.

[11]Bernasconi, M. C., and Zurbuchen, T., "Lobed Solar Sails for a Small Mission to the Asteroids," *Acta Astronautica*, Vol. 35, 1995, pp. 645–655.

[12]Main, J. A., Carlin, R. A., Garcia, E., Peterson, S. W., and Strauss, A. M., "Dynamic Analysis of Space-Based Inflated Beam Structures," *Journal of the Acoustical Society of America*, Vol. 97, No. 2, 1995, pp. 1035–1045.

[13]Engberg, B., and Lassiter, J., "Dynamic Testing of Inflatable Spacecraft Structures," *Sound and Vibration*, July 1999, pp. 16–21.

[14]Slade, K. N., and Tinker, M. L., "Analytical and Experimental Investigation of the Dynamics of Polyimide Inflatable Cylinders," *Proceedings of the 40th AIAA Structures, Structural Dynamics, and Materials Conference*, AIAA, Reston, VA, 1999, pp. 2495–2506.

[15]Pappa, R. S., Lassiter, J. O., and Ross, B. P., "Structural Dynamics Experimental Activities in Ultra-Lightweight and Inflatable Space Structures," NASA TM-2001-210857, May 2001.

[16]Lincoln, J. W., and Volterra, E., "Experimental and Theoretical Determination of Frequencies of Elastic Toroids," *Experimental Mechanics*, May 1967, pp. 211–217.

[17]Jordan, P. F., "Vibration Test of a Pressurized Torus Shell," AIAA Paper 67-73, Jan. 1967.

[18]McConnell, K. G., *Vibration Testing: Theory and Practice*, 1st ed., Wiley, New York, 1995, Chap. 5.

[19]Blevins, R. D., *Formulas for Natural Frequency and Mode Shape*, Kreiger, Malabar, FL, 1979, Chap. 9.

[20]Allemang, R. J., "Vibrations: Experimental Modal Analysis," Structural Dynamics Research Lab., Univ. of Cincinnati, Cincinnati, OH, March 1999.

[21]Banks, H. T., and Inman, D. J., "On Damping Mechanisms in Beams," *Journal of Applied Mechanics*, Vol. 58, Sept. 1991, pp. 716–723.

[22]Cudney, H. H., and Inman, D. J., "Determining Damping Mechanisms in a Composite Beam by Experimental Modal Analysis," *Journal of Modal Analysis*, Oct. 1989, pp. 138–143.

[23]Junkins, J. L., *Optimal Estimation of Dynamical Systems*, Sijthohff and Noordhoff International, Alphan aan den Rijn, The Netherlands, 1978.